remote sensing

MDPI

Article

Comparing Pre- and Post-Inversion Interpolation Strategies for Predicting Seafloor Topography

Yi Zeng [1,2], Huan Xu [3,*], Shengping Wang [1,2], Tianying Hu [4] and Chao Dong [3]

[1] School of Surveying and Geoinformation Engineering, East China University of Technology, Nanchang 330013, China; 2024100051@ecut.edu.cn (Y.Z.)
[2] Key Laboratory of Mine Environmental Monitoring and Improving Around Poyang Lake, Ministry of Natural Resources, Nanchang 330013, China
[3] Key Laboratory of Marine Environmental Survey Technology and Application, South China Sea Marine Survey Center, Ministry of Natural Resources, Guangzhou 510300, China
[4] School of Statistics and Data Science, Jiangxi University of Finance and Economics, Nanchang 330013, China
* Correspondence: xuhuan@ucas.ac.cn

Highlights

What are the main findings?

- Natural neighbor interpolation achieved the lowest RMSE among the three interpolation methods evaluated.
- Interpolating gravity anomalies before bathymetric inversion produced higher accuracy than interpolating the inverted topography afterward.

What are the implications of the main findings?

- The results may provide a reference for selecting interpolation strategies in gravity-based bathymetric inversion under similar data conditions.
- Pre-inversion interpolation can improve the use of satellite-derived marine gravity data for constructing high-resolution seafloor topography.

Abstract

Existing marine gravity anomaly models and shipborne bathymetric observations remain too coarsely resolved to support sub-kilometer mapping in sparsely surveyed waters. Local seafloor topography models at such resolutions must therefore be derived through interpolation. However, it remains unclear how inversion accuracy depends on the interpolation method and on whether interpolation is applied to gravity before inversion or to topography afterward. Using the Surface Water and Ocean Topography (SWOT) gravity anomaly model and the Gravity–Geologic Method (GGM), we compared inversion results at different target grid spacings in two 2° × 2° subregions of the Sea of Japan. Natural neighbor interpolation consistently yielded lower root-mean-square errors (RMSEs) across the tested grid spacings and better preserved local relief in complex topography. In both subregions, pre-inversion gravity interpolation outperformed post-inversion topographic interpolation at target grid spacings of 30″ and 15″. At 15″, pre-inversion gravity interpolation reduced RMSE by 10.73% in Region 1 and 15.51% in Region 2 relative to post-inversion topographic interpolation. These results indicate that, when the original gravity data have limited spatial resolution, pre-inversion gravity interpolation can be more effective than post-inversion topographic interpolation.

Keywords: seafloor topography; SWOT gravity data; interpolation strategy; distribution of shipborne bathymetric data

Check for updates

Academic Editors: Wenyu Wang, Lanjie Zhang and Zhenzhan Wang

Received: 21 October 2026
Revised: 23 November 2026
Accepted: 26 November 2026
Published: 28 November 2026

Copyright: © 2026 by the authors. Licensee MDPI, Basel, Switzerland. This article is an open access article distributed under the terms and conditions of the Creative Commons Attribution (CC BY) license.

1. Introduction

Since Marie Tharp produced the first global map of seafloor topography in 1977 [1,2], improving the accuracy and spatial resolution of global seafloor topography models has remained an important issue in geophysics. High-accuracy seafloor topographic data play an irreplaceable role in many critical fields, including marine resource exploration, ocean-current-dynamics simulation, and global climate modeling [3–5]. Although shipborne bathymetric surveying techniques can provide high-accuracy water-depth data, their insufficient survey-line coverage and high surveying costs make it difficult to meet the requirements of global seafloor topographic mapping. In contrast, marine gravity field models derived from satellite altimetry have the advantages of all-weather operation, global coverage, and low cost, and have become a key means of estimating ocean depths and filling data gaps in unsurveyed marine areas. With the continuous accumulation of altimetry missions and survey data, the inversion accuracy of marine gravity field models and global seafloor topography products is entering a new stage of comprehensive refinement [6–8].

National Aeronautics and Space Administration (NASA) conducted the first satellite altimetry experiment in 1973. After more than five decades of development, the scientific applications of satellite altimetry missions have extended far beyond the original measurement of sea surface height. Their high-precision observations have been widely applied in numerous geophysical fields, including global sea-level change monitoring, seafloor topography inversion, ocean circulation and eddy detection, and polar ice-sheet elevation monitoring [9–12]. Benefiting from the acquisition of altimetry data from the Geosat Geodetic Mission and the ERS-1 Geodetic Phase [13], Sandwell and Smith [14] constructed an early global marine gravity anomaly model. However, owing to limitations in the density of ground-track coverage, orbit determination accuracy, and data-processing capabilities at that time, its shortest resolvable wavelength was only approximately 20 km.

A review of the evolution of global seafloor topography models shows a progression from early low-resolution models, such as ETOPO5 and topo_6.2, to modern products with a grid spacing of 15″, including ETOPO 2022, SRTM15+, and GEBCO [15–17]. The improvements in their accuracy and spatial representation can primarily be attributed to the following three driving factors: (1) the continuous accumulation of shipborne bathymetric data. The integration of marine survey data has not only enriched the fundamental data available for seafloor topography but also provided essential constraints and validation benchmarks for satellite gravity-based bathymetric inversion [5,16,18]; (2) advances in satellite altimetry technology and the refinement of marine gravity field models. With the increasing number of altimetry missions and continuous improvements in measurement techniques, the ability of global marine gravity models to resolve shorter-wavelength gravity anomalies has been enhanced. In particular, observations from CryoSat-2 and Jason-1 have contributed to improvements in the accuracy and spatial resolution of marine gravity models [6,19]; and (3) improvements in inversion algorithms and the incorporation of additional geological constraints. Advances in nonlinear iterative inversion methods and the integration of prior geological information, such as sediment-related constraints, have contributed to improving the representation of complex seafloor topography [20,21].

Existing approaches to improving the accuracy and spatial representation of seafloor topography can be broadly classified into three categories. First, multi-source data integration methods combine shipborne bathymetric measurements with satellite-altimetry-derived gravity anomalies to constrain bathymetric predictions in poorly surveyed regions [16,22]. Second, physics-based inversion methods estimate seafloor topography from gravity–topography relationships in the frequency or spatial domain. Representative approaches include spectral prediction methods, the Gravity-Geologic Method (GGM), and nonlinear iterative inversion using gravity anomalies or vertical gravity gradients [20,22–24].

In addition, geological information, including sediment-related constraints, has been incorporated to improve the representation of complex seafloor features [21,25]. Third, data-driven approaches employ machine learning techniques to establish relationships between gravity observations and seafloor topography, providing alternative approaches for bathymetric prediction [26,27]. Previous comparative studies have also investigated the performance of different inversion algorithms and the effects of shipborne bathymetric data coverage [28]. However, these studies have mainly focused on data integration, inversion algorithms, and prediction models, whereas the influence of interpolation strategies within a fixed inversion framework has received relatively less attention. In particular, the effects of applying interpolation to gravity anomalies before inversion or to the recovered topography after inversion have not been sufficiently quantified under consistent experimental and validation conditions.

A significant scale mismatch remains between high-resolution seafloor topography products (15″) and the original gravity observations (1′). The relationship between gravity anomalies and seafloor topography is complex. Upward-continuation effects, subsurface geological structures, and uneven shipborne data coverage further complicate this relationship. As a result, their correlation varies across spatial scales [21,26,29]. Consequently, a large proportion of the high-frequency details in topographic models depends heavily on gridded interpolation and data-fusion processes [15,25,30]. Interpolation methods may respond differently to unevenly distributed observations. This is partly because spatial correlations vary across a study area, and local patterns may differ from regional trends [31–33]. Errors introduced by interpolation may propagate through the inversion, particularly during the separation of long- and short-wavelength gravity anomalies [27,34]. Therefore, it is important to determine which interpolation strategy produces more accurate bathymetric predictions.

To address the above issues, this study uses the Sea of Japan as the study area and investigates interpolation strategies within the GGM inversion workflow using Surface Water and Ocean Topography (SWOT) satellite gravity observations. The study has two main objectives. First, the effects of three commonly used interpolation methods—natural neighbor, kriging, and thin-plate spline—on seafloor topography inversion accuracy are compared. Second, the two strategies, pre-inversion gravity interpolation and post-inversion topographic interpolation, are systematically compared and quantitatively evaluated. To ensure a fair comparison, a spatially constrained, grid-based sampling strategy is applied to the shipborne bathymetric data to construct the control and test sets, with the same test cells retained across different grid spacings.

2. Methodology

This section primarily describes the overall methodological framework for seafloor topography inversion based on satellite gravity anomalies. Section 2.1 introduces the basic principles of GGM inversion. Section 2.2 presents the mathematical expressions for applying interpolation methods at different stages.

2.1. Gravity-Geologic Method (GGM)

The Gravity–Geologic Method (GGM) has been widely applied to topographic inversion because of its physical basis and suitability for computations involving large datasets [23]. By establishing the relationship between gravity anomalies and water depth, this method can separate the long-wavelength gravity anomalies in the region, thereby recovering the local short-wavelength gravity anomalies at unknown points and inverting the topography. Therefore, the observed gravity anomalies consist of short-wavelength

gravity anomalies caused by local seafloor relief and long-wavelength gravity anomalies caused by deep-seated effects and the regional tectonic background, as expressed below.

$$\Delta g_{obs} = \Delta g_{short} + \Delta g_{long} \quad (1)$$

where Δg_{obs} is the observed gravity anomaly at sea level, Δg_{short} is the short-wavelength gravity anomaly, and Δg_{long} is the long-wavelength gravity anomaly.

At shipborne control point j, the local short-wavelength gravity anomaly can be approximated using the simplified Bouguer slab formula as follows:

$$\Delta g_{short}(j) = 2\pi G \Delta\rho [h(j) - H] \quad (2)$$

where G is the universal gravitational constant, $\Delta\rho$ is the density contrast between seawater and the seabed material, $h(j)$ is the water depth at control point j, and H is the reference maximum water depth.

The long-wavelength gravity anomaly can be further obtained from Equation (1). Because the long-wavelength gravity field varies smoothly in space, the long-wavelength gravity anomalies at the control points can be interpolated over the entire study area, and the short-wavelength gravity anomaly $\Delta g_{short}(i)$ at the unknown point i can then be obtained. Finally, based on the linear relationship between the short-wavelength gravity anomaly and water depth, the water depth at the unknown point i can be expressed as:

$$h(i) = H + \frac{\Delta g_{short}(i)}{2\pi G \Delta\rho} \quad (3)$$

In the GGM inversion, both the reference depth H and the density contrast $\Delta\rho$ were determined adaptively. The reference depth H was defined as the maximum water depth among the shipborne control points in each study region, calculated as $H = max(h_i)$, where h_i represents the water depth at control point i. The independent test points were excluded from this calculation. The density contrast was automatically selected based on variations in inversion errors within a range of 0.5–7.0 g/cm^3, with an increment of 0.1 g/cm^3. The optimized density contrast was treated as an empirical fitting parameter rather than a direct estimate of the actual density contrast between seawater and seabed rocks [28,35,36].

It should be noted that the interpolation of long-wavelength gravity anomalies within the GGM and pre-inversion gravity interpolation serve different purposes. The former estimates long-wavelength gravity anomalies at unknown locations, whereas the latter adjusts the grid spacing of the input gravity anomaly field before inversion. In the interpolation method comparison, the same algorithm is applied to both interpolation procedures to avoid additional effects arising from the use of different interpolation algorithms.

2.2. Interpolation Operators

The interpolation performance depends not only on the algorithm itself but also on the spatial properties of the object to which it is applied. The gravity field is a geophysical response generated through potential-field integration of topography and subsurface density structures. Its spatial variations are relatively smooth and mainly contain medium- and long-wavelength information [6,22]. Shipborne bathymetric data, in contrast, exhibit pronounced local relief and high-frequency variations, particularly in complex topographic regions such as seamounts, trenches, mid-ocean ridges, and fracture zones [25]. Therefore, when interpolation operators are applied separately to the gravity field and seafloor topography, the objects being processed differ in their spatial correlation structures, spectral characteristics, and modes of error propagation.

Let the observed gravity field within the study area be denoted by $g(i,j)$, where (i,j) represents the spatial position. Let $F(\cdot)$ denote the GGM-based seafloor topography inversion operator, and let $I^{(m)}(\cdot)$ denote the m-th interpolation operator. Three methods, namely

natural neighbor interpolation, kriging interpolation, and thin-plate spline interpolation, are selected for comparison, and the following two processing pathways are constructed.

The first pathway is inversion after gravity-field interpolation; that is, the gravity-field data are first interpolated or resampled onto the target inversion grid, and GGM is then used for seafloor topography inversion. This pathway can be expressed as:

$$\hat{h}_g^{(m)} = F(I_g^{(m)} g) \tag{4}$$

where $I_g^{(m)}$ denotes the interpolation operator applied to the gravity field, and $\hat{h}_g^{(m)}$ denotes the seafloor topography obtained by first interpolating and gridding the gravity field and then performing GGM inversion.

The second pathway is topographic interpolation after direct gravity-field inversion; that is, the original gravity field is first used for GGM inversion to obtain an initial seafloor topography result, after which spatial interpolation or resampling is applied to the resulting topography. This pathway can be expressed as:

$$\hat{h}_h^{(m)} = I_h^{(m)}(F(g)) \tag{5}$$

where $I_h^{(m)}$ denotes the interpolation operator applied to the inverted seafloor topography, and $\hat{h}_h^{(m)}$ denotes the seafloor topography obtained after interpolating the inversion result.

The difference between the two processing pathways can be expressed as:

$$\Delta h^{(m)}(i,j) = \hat{h}_g^{(m)}(i,j) - \hat{h}_h^{(m)}(i,j) = \left[F\left(I_g^{(m)} g\right)\right](i,j) - \left[I_h^{(m)}(F(g))\right](i,j) \tag{6}$$

Equation (6) indicates that whether the two processing pathways are equivalent depends on whether the interpolation operator and the inversion operator satisfy the commutative relation. Because the gravity field and seafloor topography differ in terms of spatial spectra, scale support, and error structures, the following generally holds:

$$F\left(I_g^{(m)} g\right) \neq I_h^{(m)}(F(g)) \tag{7}$$

Therefore, applying interpolation in the gravity domain and the topographic domain may produce different seafloor topography inversion results. By comparing $F\left(I_g^{(m)} g\right)$ with $I_h^{(m)}(F(g))$, this study analyzes the influence of the object to which interpolation is applied on the seafloor topography inversion results. First, the three interpolation methods are compared to identify the most suitable interpolation method. Subsequently, independent shipborne bathymetric data are used for validation to evaluate the differences between the two processing pathways in terms of inversion accuracy, spatial distribution, and scale response. The workflow is shown in Figure 1.

All numerical experiments were conducted using MATLAB R2018b. Natural neighbor interpolation was implemented using a built-in MATLAB function with the 'natural' interpolation method. Ordinary kriging employed an exponential semivariogram model, with the scale parameter set to correspond to the native grid spacing of the original gravity anomaly data. The sill was determined from the variance of the input data, and neighboring samples were selected within a search radius equal to three times the scale parameter. Thin-plate spline interpolation was implemented using a built-in MATLAB function, with the smoothing parameter automatically determined for gravity-field interpolation and fixed at 0.999 for long-wavelength gravity anomaly interpolation within the GGM.

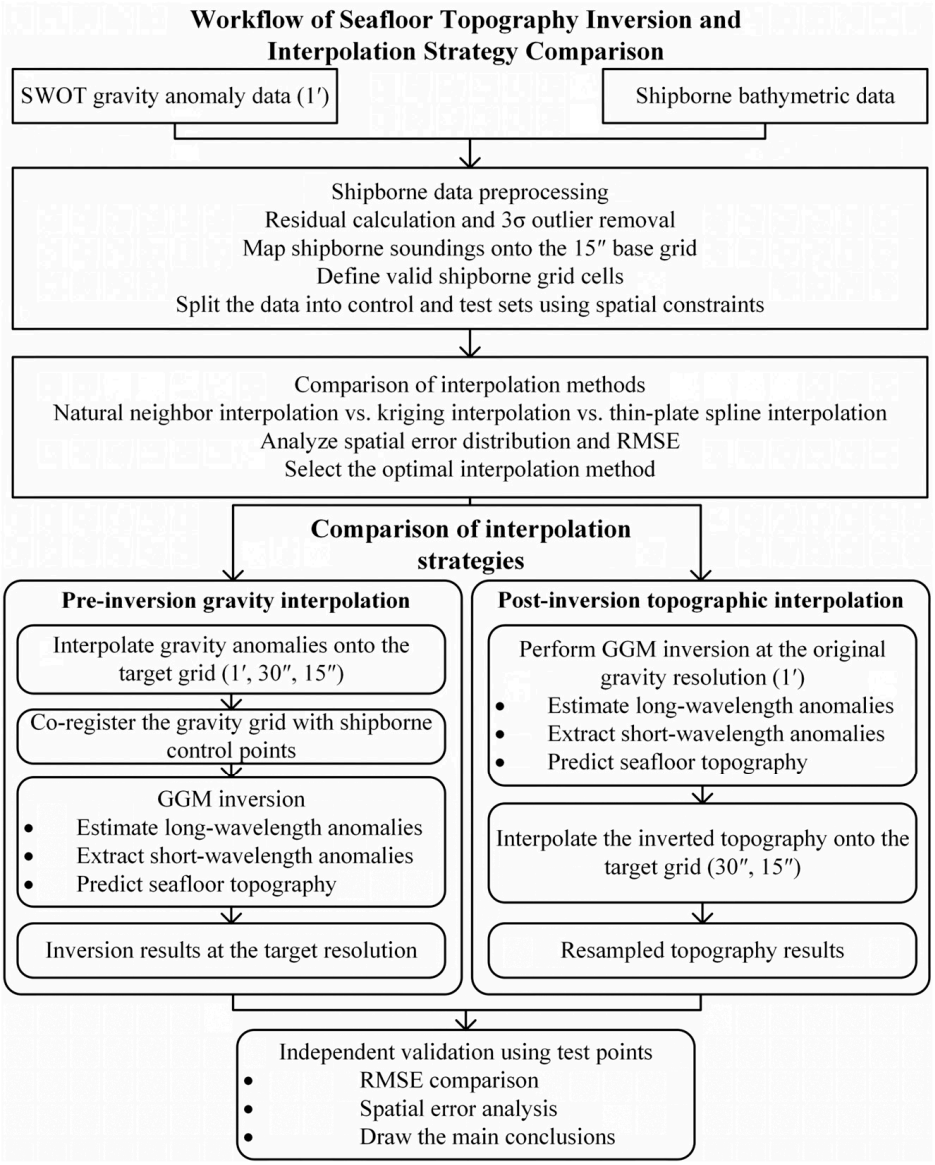

Figure 1. Overall technical workflow.

3. Data Sources

This section describes the data sources, study areas, and preprocessing procedures. Section 3.1 defines the locations of the two study areas and characterizes their topography and gravity-anomaly distributions. Section 3.2 describes the source and spatial coverage of the shipborne bathymetric data and the construction of the control and test samples.

3.1. Study Areas and SWOT Gravity Anomalies

The global marine gravity anomaly data used in this study were obtained from the SWOT_02 gravity model released by the Scripps Institution of Oceanography (SIO) in October 2024, specifically the grav_SWOT_02.nc product. The model integrates observations from the Surface Water and Ocean Topography (SWOT) satellite mission and existing satellite altimetry-derived gravity field information to improve the spatial representation of marine gravity anomalies. Compared with conventional satellite altimetry-derived gravity models, SWOT_02 incorporates wide-swath observations that improve spatial sampling and short-wavelength gravity signal recovery. Previous research has shown that repeated SWOT observations can achieve a spatial resolution of approximately 8 km and improve

sea surface slope accuracy, providing more detailed information for marine gravity field recovery [37]. The product provides gravity anomaly data in NetCDF format, with values expressed in milligals (mGal). The dataset has a native grid spacing of 1′ × 1′ and covers the global ocean region from approximately 80°S to 80°N. The data are publicly available from the SIO archive (https://topex.ucsd.edu/pub/archive/grav_SWOT/, accessed on 15 October 2026). In this study, the original 1′ gravity anomaly grid was used as the baseline, and the data were interpolated to target grid spacings of 30″ and 15″ to evaluate the effects of different interpolation strategies.

Two 2° × 2° subregions of the Sea of Japan were selected for the experiments (Figure 2). Region 1 is located in the western Sea of Japan and is characterized by relatively gentle relief and gradual variations in water depth (Figure 2a). Shipborne bathymetric observations are sparse, and the gravity anomaly field varies smoothly, with localized highs occurring only in a few areas. These characteristics allow inversion performance to be evaluated under conditions of gentle relief and limited control-point coverage. Region 2 is located in the southeastern Sea of Japan, where the seafloor topography is more complex and water depths vary over a broader range (Figure 2b). Shipborne bathymetric coverage is also denser than in Region 1. The pronounced differences in topographic relief and data coverage between the two regions provide contrasting settings for evaluating the effects of target gravity-grid spacing on the inversion results.

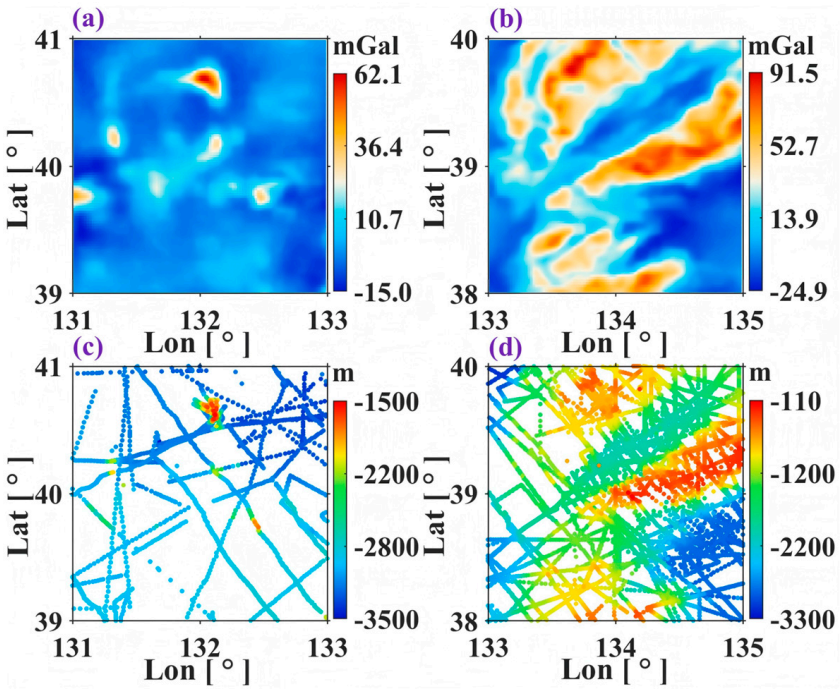

Figure 2. Study areas in the Sea of Japan. (**a**,**b**) Original gravity anomalies in Regions 1 and 2; (**c**,**d**) original shipborne bathymetric data in Regions 1 and 2.

3.2. Shipborne Bathymetric Data

Shipborne bathymetric data were obtained from National Oceanic and Atmospheric Administration (NOAA) (https://www.ncei.noaa.gov/, accessed on 15 October 2026) and used to establish control points for GGM inversion and independent test points for validation. The known water depths at the control points were used to calculate short-wavelength gravity anomalies and estimate the long-wavelength gravity anomaly field within the GGM. These observations were unevenly distributed, with locally dense and sparse coverage. We therefore refined the sample-selection procedure to improve the spatial representativeness

and independence of the control and test samples. Some existing high-resolution seafloor topography products have a grid spacing of 15″, whereas the original gravity anomaly data used in this study have a grid spacing of 1′. Therefore, we adopted 15″ as the base-grid spacing and interpolated the gravity anomaly data onto this grid, thereby establishing a consistent framework for sample partitioning.

The shipborne bathymetric observations were first spatially matched to the ETOPO1 bathymetric model, which was used as an auxiliary reference for preliminary data quality control. Residuals were then calculated between the shipborne water depths and the corresponding ETOPO1 values. Outliers in the residual sequence were identified and removed using the 3σ criterion. A total of 65 and 121 shipborne observations were removed from Regions 1 and 2, respectively. The remaining shipborne measurements were mapped onto the 15″ base grid. Grid cells containing at least one measurement were designated as valid shipborne grid cells. For grid cells containing multiple shipborne measurements, the arithmetic mean of their water depths was used as the representative depth of each cell. These cells, rather than individual measurements, served as the basic units for sample partitioning. The valid grid cells were divided into control and test sets at a ratio of 8:2, with the control cells providing bathymetric constraints for GGM inversion.

Additional spatial constraints were applied when selecting test grid cells to improve their spatial representativeness. If test cells were concentrated in densely surveyed areas, locally abundant measurements could dominate the accuracy estimates (Figure 3c). Moreover, when the grid resolution was coarsened, several adjacent test cells could be aggregated into a single cell, repeatedly representing the same area. We therefore required the minimum distance between each candidate test cell and all previously selected test cells to exceed 1′ (Figure 3b). To avoid clustering of test samples along the boundaries or in the corners, the study-area interior was defined as the area excluding the outermost grid cells. Test samples were preferentially selected from the interior and distributed as uniformly as possible. If the target number of test samples could not be reached within the interior, grid cells in the boundary region that satisfied the minimum spacing constraint were then considered. The selected cells formed the final test set, whereas all remaining valid shipborne grid cells formed the control set.

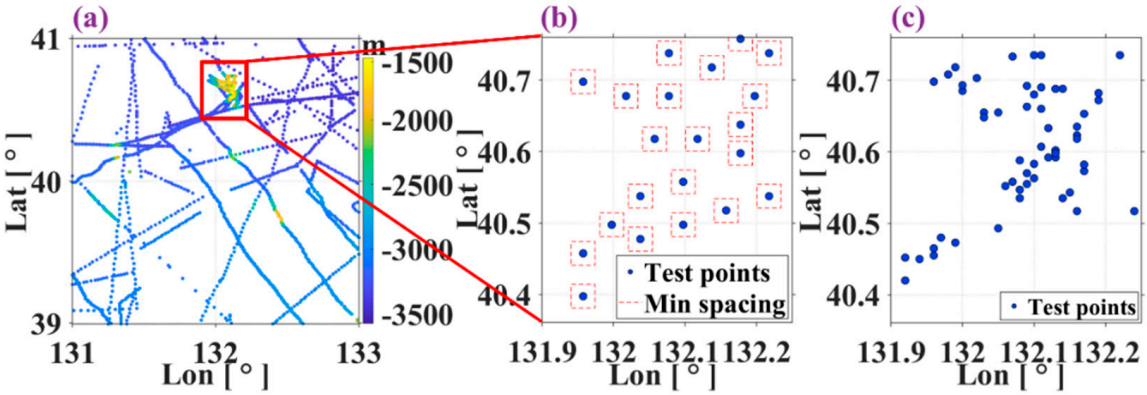

Figure 3. Distribution of shipborne bathymetric data and comparison of different test-point selection methods. (**a**) Distribution of the original shipborne bathymetric data; (**b**) distribution of test points selected using spatial constraints; (**c**) distribution of randomly selected test points.

For the multiresolution experiments, samples were initially partitioned on the 15″ base grid. At computational grid spacings of 30″ or 1′, however, multiple 15″ cells were aggregated into the same coarser grid cell. Control and test cells that were spatially independent at 15″ could therefore overlap after aggregation. If the overlapping control samples were retained, bathymetric data from the test areas would enter the GGM inversion and

compromise test-set independence. This data leakage would lead to overestimated accuracy at coarser resolutions. To prevent it, the same source test cells were retained across all coarser-resolution experiments, and control samples overlapping these cells were removed. Bathymetric information within the test cells was therefore used exclusively for accuracy assessment and excluded from the GGM inversion. Across the three target grid spacings examined in this study, 355 and 1461 test grid cells were used for accuracy assessment in Regions 1 and 2, respectively.

The original shipborne measurements followed distinct survey lines, and point density differed substantially between the two regions (Figure 4). Random partitioning would therefore concentrate both control and test samples in densely surveyed areas. The grid-based constrained method reduced the influence of spatial variations in measurement density and generated consistent sets of control and test points. This design helped ensure that differences among the experimental results arose primarily from the interpolation target or interpolation method.

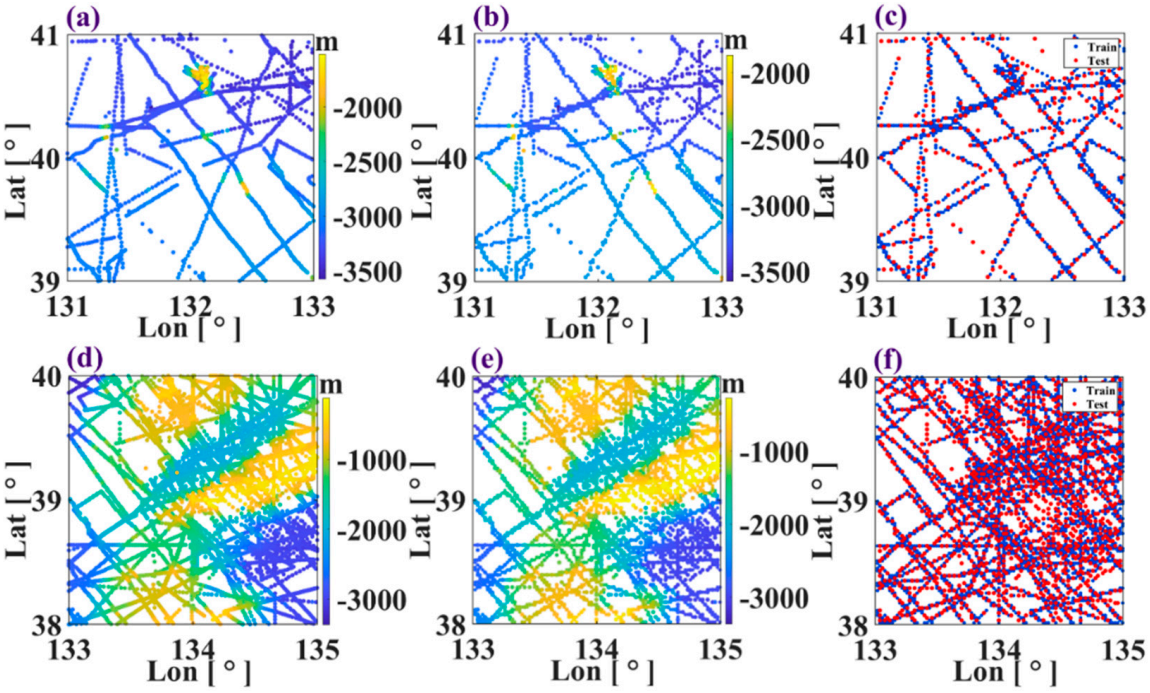

Figure 4. Distribution of shipborne data. (**a**,**d**) Original shipborne data in the two regions; (**b**,**e**) gridded shipborne data; (**c**,**f**) distributions of the control and test sets.

4. Results

4.1. Analysis of Interpolation Methods

To evaluate the effects of different interpolation methods on seafloor topography inversion accuracy, three commonly used methods, namely natural neighbor, kriging, and thin-plate spline interpolation, were compared. These methods represent local-neighborhood interpolation, spatial-statistical estimation, and smooth surface fitting, respectively. Their differences in spatial continuity, local feature preservation, and smoothing behavior may affect the estimation of long-wavelength gravity anomalies, the separation of short-wavelength components, and the resulting bathymetric predictions.

Using Region 1 as an example, all three interpolation methods recovered the principal spatial patterns and general relief characteristics of the seafloor topography (Figure 5). However, differences in the representation of local topographic features were observed. Natural neighbor interpolation preserved relatively distinct local variations and topographic

boundaries, whereas kriging produced generally continuous surfaces with smoother spatial transitions. In contrast, thin-plate spline interpolation exhibited more pronounced smoothing, resulting in reduced local topographic contrasts and less distinct small-scale features.

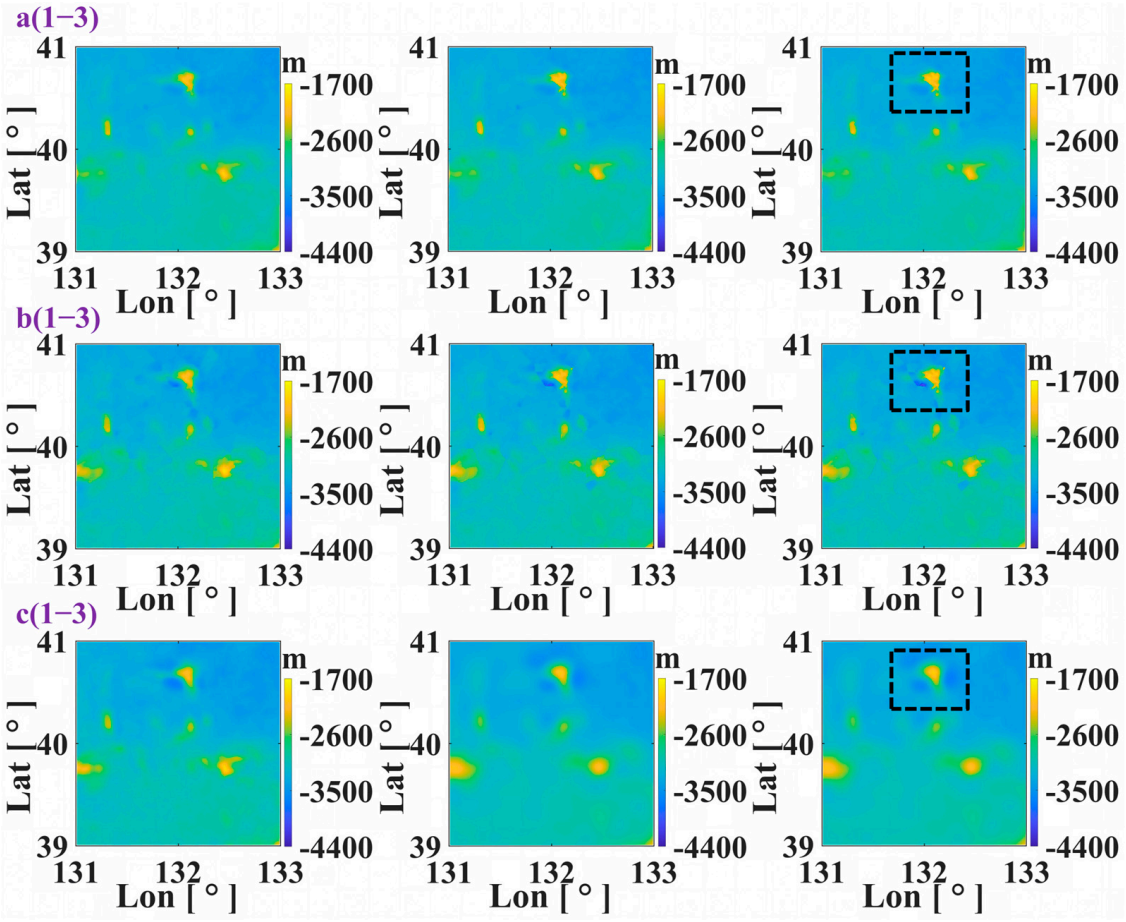

Figure 5. Seafloor topography inversion results obtained using three interpolation methods at different target grid spacings. (**a(1–3)**) Results obtained using natural neighbor interpolation at three grid spacings; (**b(1–3)**) results obtained using kriging interpolation at three grid spacings; (**c(1–3)**) results obtained using thin-plate spline interpolation at three grid spacings. The black dashed boxes highlight a representative seamount for comparison among the three interpolation methods.

To facilitate comparison, the representative seamount feature in the northern part of the study area, near 132°E and 40.7°N, is highlighted by black dashed boxes in the 15″ results (Figure 5(a3–c3)). Although the overall location and morphology of this feature were similar among the three interpolation methods, differences in its local topographic expression were evident. Natural neighbor interpolation retained relatively clear local relief, while kriging produced a smoother representation. Thin-plate spline interpolation further attenuated the local topographic variations, making the feature appear more spatially smoothed. These differences illustrate how the choice of interpolation method affects the representation of localized seafloor features.

At the original grid spacing of 1′, interpolation was applied only to estimate the long-wavelength gravity anomalies within the GGM, whereas the input gravity anomaly field retained its original grid spacing. Therefore, different interpolation methods could still produce different inversion results by affecting long-wavelength gravity anomaly estimation and subsequent short-wavelength anomaly separation. When the target gravity-grid spacing decreased from 1′ to 30″ and 15″, natural neighbor and kriging interpolation showed more noticeable changes in local topographic representation. In comparison, the thin-plate spline

results exhibited relatively limited changes across the three grid spacings, consistent with their stronger smoothing characteristics.

The spatial distributions of inversion errors are presented in Figure 6. Although most test points exhibited relatively small residuals, larger positive and negative errors were concentrated in several localized areas. In particular, the region surrounding the northern seamount, highlighted by the black dashed boxes in Figure 6(a3–c3), exhibited relatively large residuals under all three interpolation methods. Comparison with the corresponding topographic features in Figure 5 indicates that these larger errors occurred in an area of pronounced local relief, suggesting that the representation of complex topographic features remains challenging for gravity-based bathymetric inversion.

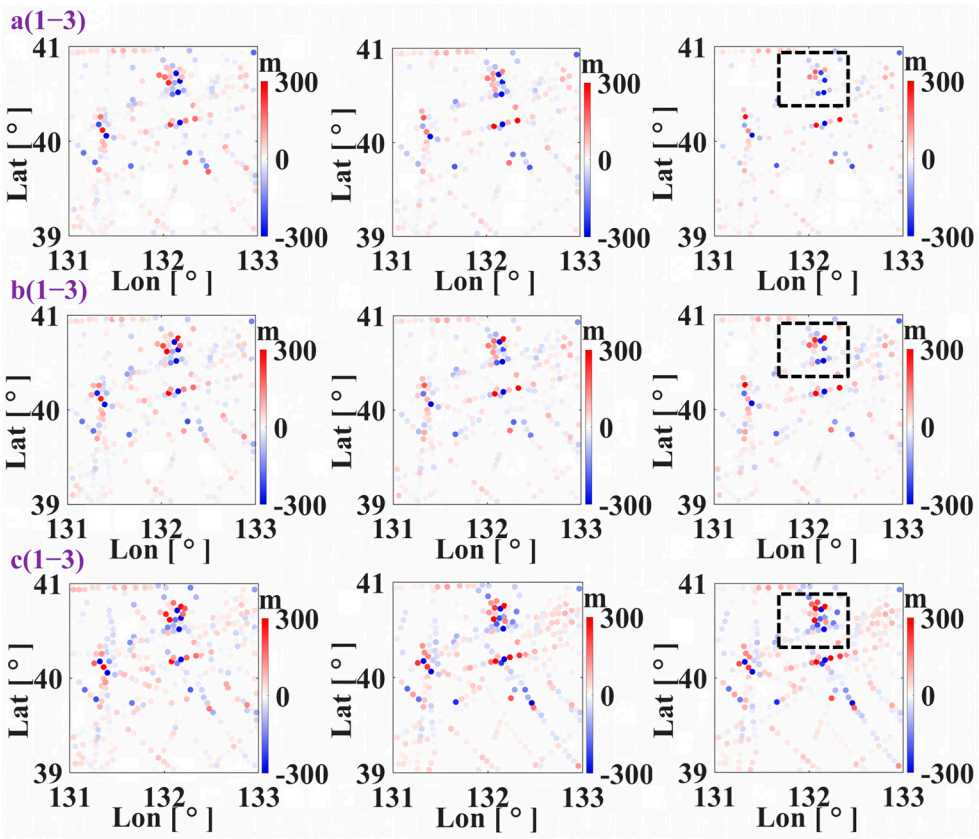

Figure 6. Error distributions of seafloor topography inversion results obtained using three interpolation methods at different target grid spacings. (**a(1–3)**) Error distributions obtained using natural neighbor interpolation at three grid spacings; (**b(1–3)**) error distributions obtained using kriging interpolation at three grid spacings; (**c(1–3)**) error distributions obtained using thin-plate spline interpolation at three grid spacings. The black dashed boxes highlight the error distributions in the seamount area shown in Figure 5.

Differences in the spatial error distributions were also observed among the three methods. Natural neighbor interpolation generally exhibited fewer pronounced residuals, while kriging showed a broadly similar spatial pattern with some localized deviations. By contrast, thin-plate spline interpolation produced more noticeable positive and negative residuals in several areas, particularly at the finer target grid spacings. These differences are consistent with the stronger smoothing of local topographic features observed in Figure 5. Nevertheless, the error patterns remained broadly similar across the tested grid spacings, indicating that finer spatial sampling alone cannot eliminate errors associated with complex topography.

The quantitative accuracy statistics are summarized in Table 1. Natural neighbor interpolation achieved the lowest RMSE and mean absolute error (MAE) at all three target grid spacings. As the grid spacing decreased from 1′ to 30″ and 15″, its RMSE decreased from 91.14 m to 83.81 m and 81.65 m, respectively, corresponding to a reduction of 10.41% from 1′ to 15″. The MAE also decreased from 38.98 m to 30.33 m. Kriging interpolation ranked second, with its RMSE decreasing from 95.10 m at 1′ to 89.46 m at 30″ and 88.54 m at 15″, representing a reduction of 6.90% from 1′ to 15″. Its MAE decreased from 40.89 m to 35.27 m over the same grid-spacing range.

Table 1. Accuracy statistics under different interpolation methods and gravity-grid spacings in Region 1.

Method	Grid Spacing	RMSE (m)	MAE (m)	Mean Bias (m)
Natural neighbor	1′	91.14	38.98	−5.32
	30″	83.81	32.91	−3.53
	15″	81.65	30.33	−2.51
Kriging	1′	95.10	40.89	−4.00
	30″	89.46	36.87	−2.53
	15″	88.54	35.27	−0.42
Thin-plate spline	1′	104.62	50.62	−2.65
	30″	105.00	52.76	1.71
	15″	104.72	52.67	0.95

In contrast, thin-plate spline interpolation did not exhibit a consistent improvement in prediction accuracy as the target grid spacing decreased. Its RMSE values were 104.62 m, 105.00 m, and 104.72 m at 1′, 30″, and 15″, respectively, while the corresponding MAE values were 50.62 m, 52.76 m, and 52.67 m. Compared with the original 1′ results, the RMSE increased by only 0.38 m and 0.10 m at 30″ and 15″, respectively, indicating relatively small, non-monotonic variations rather than a substantial degradation in accuracy. This behavior may be related to the smoothing characteristics of thin-plate spline interpolation, as illustrated by the relatively smooth local topographic features in Figure 5. In the GGM workflow, thin-plate spline interpolation is applied both to the input gravity anomaly field and to the estimation of long-wavelength gravity anomalies. Its smoothing effect may attenuate local gravity variations and influence the separation of long- and short-wavelength components, leading to small fluctuations in the resulting bathymetric prediction errors. Thus, a finer target grid does not always improve prediction accuracy, especially when interpolation smooths out local variations.

Across the three target grid spacings, the mean RMSE values were 85.53 m, 91.03 m, and 104.78 m for natural neighbor, kriging, and thin-plate spline interpolation, respectively. The mean RMSE of natural neighbor interpolation was therefore 18.37% lower than that of thin-plate spline interpolation and 6.04% lower than that of kriging. The MAE results were consistent with the RMSE comparison, confirming the overall accuracy advantage of natural neighbor interpolation under the examined conditions. Meanwhile, the mean bias values of all three methods remained relatively small compared with their corresponding RMSE values, indicating limited overall systematic bias despite the presence of relatively large local residuals.

Overall, the visual comparisons in Figures 5 and 6 and the quantitative statistics in Table 1 demonstrate that interpolation methods affect both the spatial representation and prediction accuracy of seafloor topography. Natural neighbor interpolation achieved the lowest RMSE and MAE across all tested grid spacings and better preserved local topographic

variations. Therefore, it was selected for the subsequent comparison of pre-inversion gravity interpolation and post-inversion topographic interpolation.

4.2. Analysis of Interpolation Objects

A spatial-scale mismatch exists between gravity anomalies and seafloor topography. Available gravity anomaly data have comparatively coarse native resolution, whereas existing seafloor topography products resolve finer spatial structures. Improving gravity-derived bathymetry therefore requires determining whether interpolation should be applied to the input gravity field or the inverted topography. To address this question, we evaluated two schemes: gravity interpolation and topographic interpolation.

Under the gravity interpolation scheme, the original gravity anomalies were first interpolated onto the target-resolution grid and co-registered with the shipborne control points. The GGM workflow was then applied to estimate the long-wavelength anomaly, extract the short-wavelength component, and invert for water depth. Under the topographic interpolation scheme, GGM inversion was first performed at the native gravity resolution. The resulting topography was subsequently interpolated onto the target-resolution grid.

Decreasing the target grid spacing of the input gravity field from 1′ to 30″ and 15″ progressively sharpened the inverted topography, revealing finer relief and clearer topographic boundaries (Figure 7). In gently varying Region 1, the broad topographic pattern remained stable, whereas local anomalies became more distinct. Improvements were more pronounced in Region 2, with clearer topographic textures and local extrema. The enhanced spatial definition was accompanied by lower inversion errors in both regions (Figure 8). Errors in Region 1 remained generally small and were concentrated where the topography varied rapidly. Region 2 showed a broader error distribution, including pronounced positive and negative residuals in several areas of rugged relief. The systematic reduction in error with decreasing input grid spacing suggests that pre-inversion gravity interpolation enables more effective utilization of the existing gravity and bathymetric constraints within the GGM.

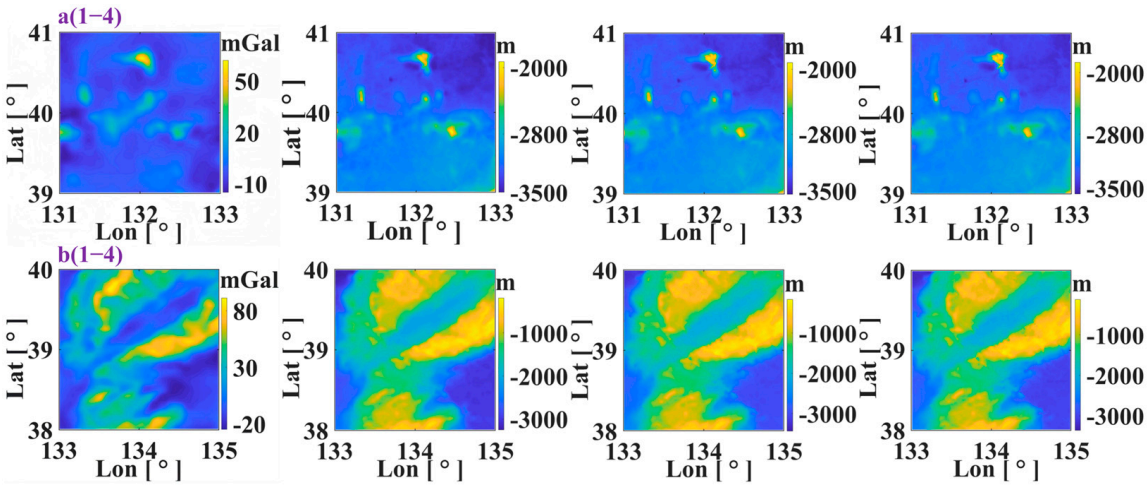

Figure 7. Inversion results obtained by interpolating the gravity data onto grids with different target spacings. (**a(1–4)**) Original gravity anomaly in Region 1 and the inversion results at the three target grid spacings; (**b(1–4)**) original gravity anomaly in Region 2 and the inversion results at the three target grid spacings.

By contrast, under the topographic-interpolation scheme, GGM inversion was performed at 1′ and the resulting topography was subsequently resampled to 30″ and 15″ (Figure 9). Resampling produced smoother and more continuous maps but preserved the principal topographic pattern of the original 1′ solution, introducing little additional

spatial structure. This limited change contrasts with the progressive refinement achieved by decreasing the target grid spacing of the input gravity field. The error distributions at 30″ and 15″ were likewise nearly unchanged, with the largest residuals persisting in areas of pronounced relief (Figure 10). Thus, topographic interpolation increased the sampling density without materially strengthening the physical constraints on GGM inversion or improving its accuracy. These results distinguish enhanced map continuity from the genuine recovery of short-wavelength topographic information.

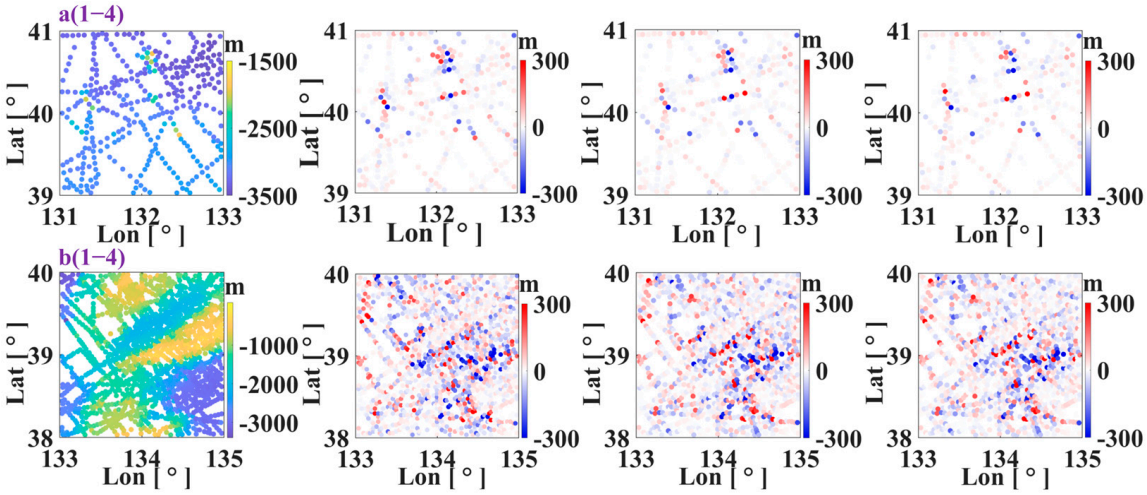

Figure 8. Error distributions obtained by interpolating the gravity data onto grids with different target spacings. (**a**(**1–4**)) Distribution of the test set in Region 1 and the error distributions at the three target grid spacings; (**b**(**1–4**)) distribution of the test set in Region 2 and the error distributions at the three target grid spacings.

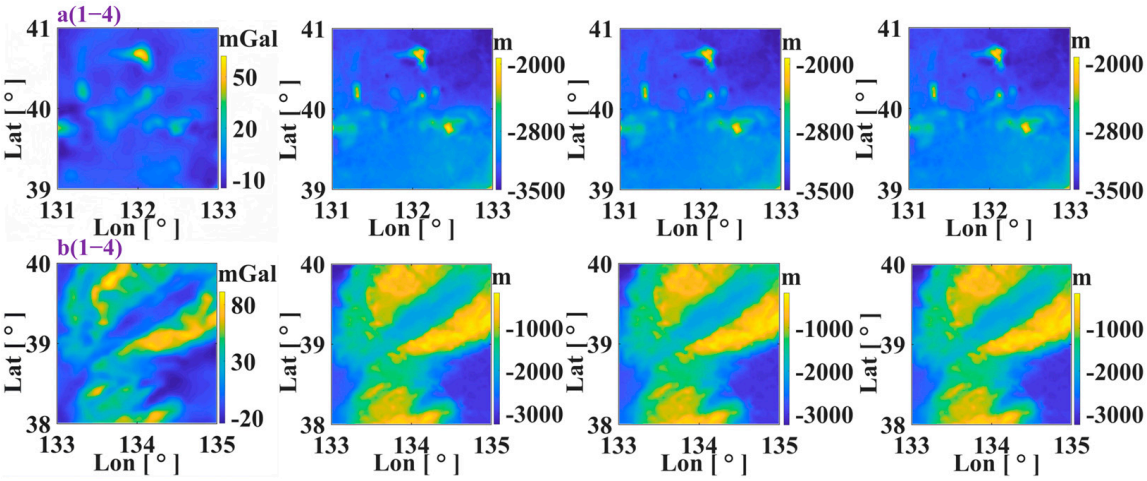

Figure 9. Results obtained by interpolating the inverted topography onto grids with different target spacings. (**a**(**1–4**)) Original gravity anomaly in Region 1 and the results at the three target grid spacings; (**b**(**1–4**)) original gravity anomaly in Region 2 and the results at the three target grid spacings.

Gravity interpolation yielded progressively lower RMSE values at finer target grid spacings in both regions (Table 2). In Region 1, the RMSE decreased from 91.14 m at 1′ to 83.81 m at 30″ and 81.65 m at 15″, corresponding to a 10.41% reduction from 1′ to 15″. The decrease was more pronounced in Region 2, where the RMSE fell from 108.29 m at 1′ to 94.25 m at 30″ and 91.43 m at 15″. This represents a 15.57% reduction relative to the 1′ result. The differences in accuracy improvement between the two study regions may be

influenced by multiple factors, including topographic relief, spatial variations in gravity anomalies, and shipborne bathymetric data coverage.

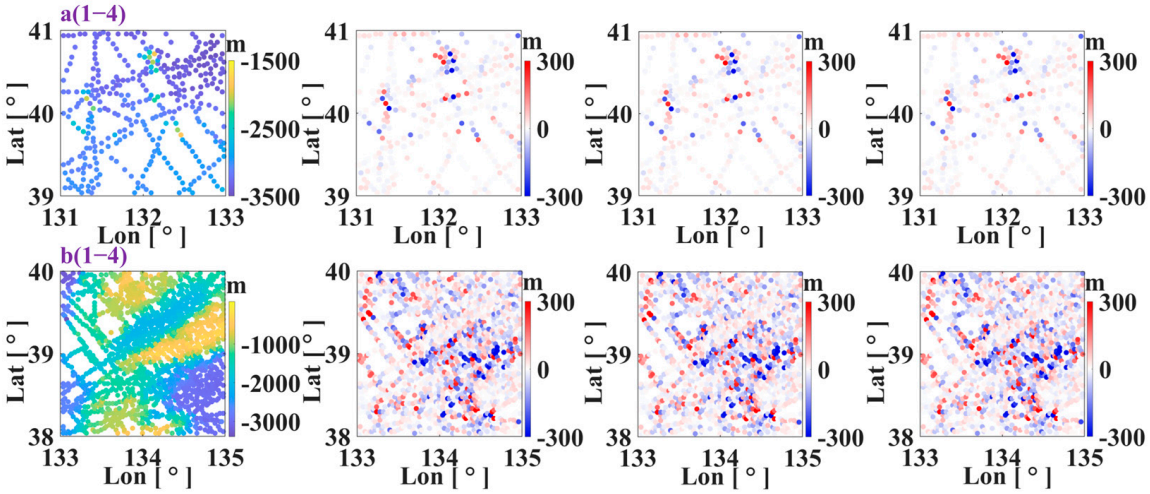

Figure 10. Error distributions obtained by interpolating the inverted topography onto grids with different target spacings. (**a**(**1–4**)) Distribution of the test set in Region 1 and the error distributions at the three target grid spacings; (**b**(**1–4**)) distribution of the test set in Region 2 and the error distributions at the three target grid spacings.

Table 2. Accuracy comparison of different interpolation strategies and existing bathymetric models.

Region	Model	Grid Spacing	RMSE (m)	MAE (m)	Mean Bias (m)
1	Gravity interpolation	1′	91.14	38.98	−5.32
		30″	83.81	32.91	−3.53
		15″	81.65	30.33	−2.51
	Topographic interpolation	30″	91.64	38.63	−4.39
		15″	91.46	37.48	−3.74
	ETOPO1	1′	121.72	63.45	13.24
	SRTM15+	15″	57.44	22.38	8.69
	GEBCO 2024	15″	72.83	31.83	19.44
2	Gravity interpolation	1′	108.29	65.67	−4.30
		30″	94.25	52.59	−3.02
		15″	91.43	49.78	−2.83
	Topographic interpolation	30″	108.18	61.49	−3.98
		15″	108.21	60.65	−4.24
	ETOPO1	1′	151.27	101.04	−16.68
	SRTM15+	15″	93.37	46.25	0.11
	GEBCO 2024	15″	101.90	51.89	4.27

However, under the topographic interpolation scheme, the RMSE changed only slightly despite the decrease in target grid spacing. The RMSE values at 30″ and 15″ were 91.64 m and 91.46 m in Region 1, compared with 108.18 m and 108.21 m in Region 2. The MAE results were consistent with the RMSE results, with pre-inversion gravity interpolation achieving lower RMSE and MAE values in both regions at a grid spacing of 15″. This indicates that interpolating the input gravity anomalies onto a finer grid before inversion is more effective in improving inversion accuracy than interpolating the inverted topography afterward.

To further evaluate the accuracy of the inversion results, the 15″ results obtained using pre-inversion gravity interpolation were compared with three existing bathymetric

models: SRTM15+, GEBCO 2024 [38], and ETOPO1 (Table 2). In Region 1, SRTM15+ and GEBCO 2024 achieved RMSE values of 57.44 m and 72.83 m, respectively, both lower than the 81.65 m obtained in this study. However, the results of this study exhibited a lower MAE than GEBCO 2024 and the smallest absolute mean bias among the four models. In Region 2, the results of this study achieved the lowest RMSE of 91.43 m, compared with 93.37 m for SRTM15+, 101.90 m for GEBCO 2024, and 151.27 m for ETOPO1. The MAE of this study was lower than those of GEBCO 2024 and ETOPO1 but slightly higher than that of SRTM15+. It should be noted that existing bathymetric models incorporate shipborne bathymetric observations, and potential overlap between their source data and the bathymetric observations used for validation in this study cannot be completely excluded. Such data overlap may affect the comparative accuracy statistics and may partly explain the lower RMSE values of the reference bathymetric models in Region 1. Nevertheless, the results of this study consistently outperformed ETOPO1 in terms of RMSE and MAE in both regions.

We further investigated the factors affecting bathymetric inversion accuracy by examining the relationships between inversion errors and topographic slope, gravity anomaly gradient, and shipborne bathymetric control-point density. The results showed that topographic slope had the strongest positive correlation with absolute inversion errors, with larger slopes generally associated with greater errors. In addition, the gravity anomaly gradient and shipborne control-point density also affected inversion accuracy. Therefore, bathymetric inversion errors are not determined by a single factor but are influenced by the combined effects of topographic complexity, spatial variations in the gravity field, and the distribution of shipborne bathymetric data.

5. Discussion and Conclusions

To address the resolution mismatch between gravity data and topographic products, we systematically compared the effects of different interpolation methods and interpolation objects on seafloor topography inversion. The results show that interpolation affected spatial sampling, long-wavelength gravity estimation, short-wavelength anomaly separation, and final water-depth accuracy.

Reliable comparison among experiments requires spatially independent validation data. Shipborne observations are unevenly distributed along survey lines, so random point-level partitioning can place control and test samples close together and underestimate test errors. To reduce this bias, we used grid cells containing shipborne measurements as partitioning units and imposed a minimum-spacing constraint between test cells. This strategy distributed the test samples more widely and increased the spatial independence of the control and test sets. Retaining the same test samples across resolutions also prevented repartitioning from changing the evaluation criteria, enabling more objective comparisons among interpolation approaches.

Different representations of the spatial field led to differences in the inversion results. Kriging is constrained by spatial autocorrelation and therefore provides stable estimates, but it tends to smooth areas lacking observational control. This smoothing weakens the representation of local short-wavelength topography. Thin-plate spline interpolation generates a smooth and continuous long-wavelength field, but its global smoothness constraint suppresses local short-wavelength anomalies and complex topographic details. Natural neighbor interpolation relies on nearby observations, helping to preserve local spatial variations and reduce excessive smoothing. Under the data conditions examined here, natural neighbor interpolation therefore better preserved local seafloor relief and achieved higher water-depth accuracy.

The effects of different interpolation objects depend on where high-resolution spatial representation is introduced into the inversion workflow. Gravity anomalies provide the primary constraints on seafloor relief, particularly through short-wavelength signals associated with local topographic variations. These signals are especially important for inversion in areas of complex relief. When low-resolution gravity data inadequately represent them, densifying the inverted topography can improve spatial continuity but cannot readily restore missing topographic details. Furthermore, at coarser grid resolutions, multiple shipborne bathymetric observations may be aggregated into the same grid cell, weakening the spatial distribution information of the bathymetric constraints. By contrast, pre-inversion gravity interpolation places gravity anomalies and shipborne control points on a finer common grid. This allows the GGM to use the available bathymetric constraints more effectively when estimating long-wavelength anomalies and separating short-wavelength components.

Interpolation can improve spatial representation but cannot create new observational information. Its effectiveness therefore remains limited by the accuracy and resolution of the original gravity data. In areas of pronounced relief or complex geology, the original gravity anomalies may not adequately capture local topographic variations. Under these conditions, interpolation alone cannot fully recover the details of complex seafloor topography. This limitation is also reflected in the larger inversion errors observed in areas with steeper seafloor slopes. In addition to the limitations of interpolation methods, the simplified Bouguer slab approximation and the assumption of a constant density contrast in the GGM may also introduce uncertainties into the inversion. The density distribution in actual marine geological environments is generally spatially heterogeneous, particularly in regions containing high-density minerals, low-density sedimentary layers, or complex geological structures. In such regions, observed gravity anomalies are influenced not only by seafloor relief but also by gravity signals arising from variations in subsurface density structures. These factors may also affect the separation of long- and short-wavelength gravity anomalies, causing the gravitational effects of density anomalies to be incorrectly interpreted as variations in seafloor topography.

Furthermore, the selection of the reference water depth and the estimation of long-wavelength gravity anomalies may introduce additional uncertainties. Particularly in areas with sparse shipborne control points, limited observational constraints may further affect the final inversion results. Potential positioning errors in historical shipborne bathymetric data may also affect inversion accuracy, particularly in areas with steep seafloor relief. Future studies could mitigate these uncertainties by examining historical cruise navigation metadata and incorporating more recent multibeam bathymetric observations as inversion control points and independent validation data.

In summary, we evaluated three interpolation methods and two interpolation objects across two 2° × 2° subregions in the Sea of Japan. Shipborne bathymetric data were used to validate the inversion results. The three interpolation methods differed in both overall accuracy and stability. Natural neighbor interpolation produced relatively low RMSE values under most experimental conditions and was therefore more suitable for the data examined in this study. Gravity interpolation generally outperformed topographic interpolation, indicating that the interpolation object substantially affected inversion accuracy. When gravity-data resolution was limited, improving the spatial representation of the gravity field before inversion was more effective than densifying the inverted topography.

Together, these results show that both the interpolation method and interpolation object influence seafloor topography inversion when gravity data and topographic products differ in spatial resolution. The results provide a reference for refined seafloor topography inversion under such resolution mismatches. Future studies should combine more accurate gravity data with additional representative marine regions to further assess the

applicability of this approach. In addition, the use of vertical gravity gradient (VGG) data within an appropriate inversion framework could be investigated to further evaluate the effects of different interpolation strategies on the recovery of short-wavelength seafloor topographic features.

Author Contributions: Software, numerical experiments, analysis of the computational results, and writing—original draft, Y.Z.; derivation of the main equations, design of the numerical experiments, and writing—review and editing, H.X. and S.W.; analysis of the bathymetric data and writing—review and editing, T.H. and C.D. All authors have read and agreed to the published version of the manuscript.

Funding: This research was supported by the Key Research Project of China Railway Group Limited (No. 2026-key-16), the National Natural Science Foundation of China (No. 42604077), the Key Laboratory of Marine Environmental Survey Technology and Application, Ministry of Natural Resources, Open Fund Project (No. MESTA-2023-A003), the Graduate Student Innovation Fund Project of East China University of Technology (No. DHYC-2025002), and the National Precision Gravity Measurement Science Center Development Foundation (No. 2025011).

Data Availability Statement: The gravity field data are from the SIO public data (https://topex.ucsd.edu/pub/archive/grav_SWOT/, accessed on 15 October 2026); ship sounding data are from the NOAA public data (https://www.ncei.noaa.gov/, accessed on 15 October 2026).

Conflicts of Interest: The authors declare no conflicts of interest.

References

1. North, G.W. Marie Tharp: The lady who showed us the ocean floors. *Phys. Chem. Earth* **2010**, *35*, 881–886. [CrossRef]
2. Barton, C. Marie Tharp, oceanographic cartographer, and her contributions to the revolution in the Earth sciences. *Geol. Soc. Lond. Spec. Publ.* **2002**, *192*, 215–228. [CrossRef]
3. Gille, S.T.; Metzger, E.J.; Tokmakian, R. Seafloor topography and ocean circulation. *Oceanography* **2004**, *17*, 47–54. [CrossRef]
4. Jayne, S.R.; St. Laurent, L.C.; Gille, S.T. Connections between ocean bottom topography and Earth's climate. *Oceanography* **2004**, *17*, 65–74. [CrossRef]
5. Wölfl, A.C.; Snaith, H.; Amirebrahimi, S.; Devey, C.W.; Dorschel, B.; Ferrini, V.; Huvenne, V.A.I.; Jakobsson, M.; Jencks, J.; Johnston, G.; et al. Seafloor mapping: The challenge of a truly global ocean bathymetry. *Front. Mar. Sci.* **2019**, *6*, 283. [CrossRef]
6. Sandwell, D.T.; Harper, H.; Tozer, B.; Smith, W.H. Gravity field recovery from geodetic altimeter missions. *Adv. Space Res.* **2021**, *68*, 1059–1072. [CrossRef]
7. Mayer, L.; Jakobsson, M.; Allen, G.; Dorschel, B.; Falconer, R.; Ferrini, V.; Lamarche, G.; Snaith, H.; Weatherall, P. The Nippon Foundation—GEBCO Seabed 2030 Project: The Quest to See the World's Oceans Completely Mapped by 2030. *Geosciences* **2018**, *8*, 63. [CrossRef]
8. Xu, H.; Wang, Q.; Yu, J.; Anderson, O.B.; Tian, Y.; Xu, N. Topography prediction from marine gravity and satellite imagery and ship soundings. *Geophys. J. Int.* **2025**, *241*, 919–933. [CrossRef]
9. Douglas, B.C.; McAdoo, D.C.; Cheney, R.E. Oceanographic and geophysical applications of satellite altimetry. *Rev. Geophys.* **1987**, *25*, 875–880. [CrossRef]
10. Leitao, C.D.; McGoogan, J.T. Skylab radar altimeter: Short-wavelength perturbations detected in ocean surface profiles. *Science* **1974**, *186*, 1208–1209. [CrossRef] [PubMed]
11. Le Traon, P.-Y.; Dibarboure, G.; Lellouche, J.-M.; Pujol, M.-I.; Benkiran, M.; Drevillon, M.; Drillet, Y.; Faugère, Y.; Remy, E. Satellite altimetry and operational oceanography: From Jason-1 to SWOT. *Ocean Sci.* **2025**, *21*, 1329–1347. [CrossRef]
12. Nilsson, B.; Andersen, O.B.; Knudsen, P. Assessment of the performance of SWOT for observing the static ocean topography. *Geophys. Res. Lett.* **2025**, *52*, e2024GL112290. [CrossRef]
13. Andersen, O.B.; Knudsen, P. Global marine gravity field from the ERS-1 and Geosat geodetic mission altimetry. *J. Geophys. Res. Ocean.* **1998**, *103*, 8129–8137. [CrossRef]
14. Sandwell, D.T.; Smith, W.H.F. Marine gravity anomaly from Geosat and ERS-1 satellite altimetry. *J. Geophys. Res. Solid Earth* **1997**, *102*, 10039–10054. [CrossRef]
15. Weatherall, P.; Marks, K.M.; Jakobsson, M.; Schmitt, T.; Tani, S.; Arndt, J.E.; Rovere, M.; Chayes, D.; Ferrini, V.; Wigley, R. A new digital bathymetric model of the world's oceans. *Earth Space Sci.* **2015**, *2*, 331–345. [CrossRef]
16. Tozer, B.; Sandwell, D.T.; Smith, W.H.F.; Olson, C.; Beale, J.R.; Wessel, P. Global Bathymetry and Topography at 15 Arc Sec: SRTM15+. *Earth Space Sci.* **2019**, *6*, 1847–1864. [CrossRef]

17. MacFerrin, M.; Amante, C.; Carignan, K.; Love, M.; Lim, E. The Earth Topography 2022 (ETOPO 2022) global DEM dataset. *Earth Syst. Sci. Data* **2025**, *17*, 1835–1849. [CrossRef]
18. Becker, J.J.; Sandwell, D.T.; Smith, W.H.F.; Braud, J.; Binder, B.; Depner, J.; Fabre, D.; Factor, J.; Ingalls, S.; Kim, S.-H.; et al. Global Bathymetry and Elevation Data at 30 Arc Seconds Resolution: SRTM30 PLUS. *Mar. Geod.* **2009**, *32*, 355–371. [CrossRef]
19. Sandwell, D.T.; Müller, R.D.; Smith, W.H.F.; Garcia, E.; Francis, R. New global marine gravity model from CryoSat-2 and Jason-1 reveals buried tectonic structure. *Science* **2014**, *346*, 65–67. [CrossRef] [PubMed]
20. Fan, D.; Li, S.; Li, X.; Yang, J.; Wan, X. Seafloor Topography Estimation from Gravity Anomaly and Vertical Gravity Gradient Using Nonlinear Iterative Least Square Method. *Remote Sens.* **2021**, *13*, 64. [CrossRef]
21. Jiang, X.; Jiang, T.; Guo, J.; Ge, B. Incorporating Sediment Effects Into Seafloor Topographic Inversion via Coefficient-Constrained Multivariate Regression. *IEEE Trans. Geosci. Remote Sens.* **2025**, *63*, 4206912. [CrossRef]
22. Smith, W.H.F.; Sandwell, D.T. Global Sea Floor Topography from Satellite Altimetry and Ship Depth Soundings. *Science* **1997**, *277*, 1956–1962. [CrossRef]
23. Kim, J.W.; von Frese, R.R.B.; Lee, B.Y.; Roman, D.R.; Doh, S.-J. Altimetry-Derived Gravity Predictions of Bathymetry by the Gravity-Geologic Method. *Pure Appl. Geophys.* **2011**, *168*, 815–826. [CrossRef]
24. Xu, H.; Yu, J. Using an iterative algorithm to predict topography from vertical gravity gradients and ship soundings. *Earth Space Sci.* **2022**, *9*, e2022EA002437. [CrossRef]
25. Sandwell, D.T.; Goff, J.A.; Gevorgian, J.; Harper, H.; Kim, S.; Yu, Y.; Tozer, B.; Wessel, P.; Smith, W.H.F. Improved Bathymetric Prediction Using Geological Information: SYNBATH. *Earth Space Sci.* **2022**, *9*, e2021EA002069. [CrossRef]
26. Yang, L.; Liu, M.; Liu, N.; Guo, J.; Lin, L.; Zhang, Y.; Du, X.; Xu, Y.; Zhu, C.; Wang, Y. Recovering Bathymetry From Satellite Altimetry-Derived Gravity by Fully Connected Deep Neural Network. *IEEE Geosci. Remote Sens. Lett.* **2023**, *20*, 1502805. [CrossRef]
27. Ge, B.; Guo, J.; Kong, Q.; Zhu, C.; Huang, L.; Sun, H.; Liu, X. Seafloor topography inversion from multi-source marine gravity data using multi-channel convolutional neural network. *Eng. Appl. Artif. Intell.* **2025**, *139*, 109567. [CrossRef]
28. Tian, Y.; Xu, H.; Yu, J.; Wang, Q.; Jia, Y.; Chen, X. Comparative Study of Seafloor Topography Prediction from Gravity–Geologic Method and Analytical Algorithm. *Remote Sens.* **2024**, *16*, 3154. [CrossRef]
29. Hu, T.; Liu, X.; Wang, C.; Yang, Z.; Dong, C.; Xu, H. Gravity-Geological Method for Seafloor Topography Inversion Considering Spatial Heterogeneity. *Mar. Geod.* **2025**, *49*, 567–584. [CrossRef]
30. Marks, K.M.; Smith, W.H.F. An Evaluation of Publicly Available Global Bathymetry Grids. *Mar. Geophys. Res.* **2006**, *27*, 19–34. [CrossRef]
31. Sampson, P.D.; Guttorp, P. Nonparametric Estimation of Nonstationary Spatial Covariance Structure. *J. Am. Stat. Assoc.* **1992**, *87*, 108–119. [CrossRef]
32. Tobler, W.R. A computer movie simulating urban growth in the Detroit region. *Econ. Geogr.* **1970**, *46*, 234–240. [CrossRef] [PubMed]
33. Goodchild, M.F. The validity and usefulness of laws in geographic information science and geography. *Ann. Assoc. Am. Geogr.* **2004**, *94*, 300–303. [CrossRef]
34. Heaton, M.J.; Datta, A.; Finley, A.O.; Furrer, R.; Guinness, J.; Guhaniyogi, R.; Gerber, F.; Gramacy, R.B.; Hammerling, D.; Katzfuss, M.; et al. A Case Study Competition Among Methods for Analyzing Large Spatial Data. *J. Agric. Biol. Environ. Stat.* **2019**, *24*, 398–425. [CrossRef] [PubMed]
35. Kim, K.B.; Hsiao, Y.-S.; Kim, J.W.; Lee, B.Y.; Kwon, Y.K.; Kim, C.H. Bathymetry enhancement by altimetry-derived gravity anomalies in the East Sea (Sea of Japan). *Mar. Geophys. Res.* **2010**, *31*, 285–298. [CrossRef]
36. Jiang, X.; Guo, J.; Lin, M.; Sun, H.; Jiang, T. Enhanced gravity-geologic method to predict bathymetry by considering non-linear effects of surrounding seafloor topography. *Geophys. J. Int.* **2024**, *239*, 754–767. [CrossRef]
37. Yu, Y.; Sandwell, D.T.; Dibarboure, G.; Chen, C.; Wang, J. Accuracy and resolution of SWOT altimetry: Foundation seamounts. *Earth Space Sci.* **2024**, *11*, e2024EA003581. [CrossRef]
38. GEBCO Compilation Group. *The GEBCO_2024 Grid—A Continuous Terrain Model of the Global Oceans and Land*; NERC EDS British Oceanographic Data Centre NOC: Liverpool, UK, 2024. [CrossRef]

Disclaimer/Publisher's Note: The statements, opinions and data contained in all publications are solely those of the individual author(s) and contributor(s) and not of MDPI and/or the editor(s). MDPI and/or the editor(s) disclaim responsibility for any injury to people or property resulting from any ideas, methods, instructions or products referred to in the content.